

# Hydrodynamic simulations of the colliding winds in Iota Orionis

Julian M. Pittard<sup>★</sup>

*School of Physics and Astronomy, University of Birmingham, Edgbaston, Birmingham B15 2TT*

Accepted 1998 June 12. Received 1998 May 20; in original form 1997 December 15

## ABSTRACT

Two-dimensional hydrodynamic simulations of the colliding winds in the eccentric binary Iota Orionis (HR 1889; HD 37043) have been conducted. With the inclusion of radiative driving, the realistic simulation of such a system becomes possible for the first time. The dynamics of the post-shock flow throughout the orbit are explored. Radiative inhibition and sudden radiative braking both occur, lowering the temperature of the post-shock gas. Instabilities in the collision region are ubiquitous, leading to a great deal of structure. Two separate models with different stellar mass-loss rates are examined. In both models the colliding wind shock collapses on to the photosphere of the secondary around periastron, owing to the imbalance between the wind momentum fluxes. However, the shock is able to detach from the surface of the secondary in the less extreme model as the secondary star heads towards apastron. A higher resolution simulation indicates that this result is currently resolution-dependent.

The synthetic intrinsic X-ray emission is extremely dependent on the amount of cooling in the post-shock flow, and hence its nature changes substantially if the shock detaches. In such a case it is very soft at periastron, but much harder at apastron. During the former, the secondary star penetrates deep into the wind acceleration region of the primary, and the pre-shock velocity is reduced from  $\sim 2000$  to  $\sim 1000$  km s<sup>-1</sup>. The post-shock density also substantially increases, resulting in very strong cooling. In comparison, at apastron the post-shock density is low, and the pre-shock velocity is high, resulting in a very adiabatic wind collision. Synthetic X-ray light curves show a minimum in the 0.4–10.0 keV *ASCA* band centred on periastron with a duration of a couple of days. If the shock detaches, a reduction in the 0.1–0.5 keV *ROSAT* emission is also predicted. Such variation, if seen in ‘real’ data, may help in accurately determining the mass-loss rates of the stellar components.

**Key words:** hydrodynamics – shock waves – binaries: general – stars: individual: Iota Orionis (HD 37043) – stars: mass-loss – X-rays: stars.

## 1 INTRODUCTION

The numerical modelling of colliding stellar winds is a relatively recent area of study (e.g. Luo, McCray & Mac Low 1990; Stevens, Blondin & Pollock 1992). As such, the models used to date have, for the most part, been relatively unsophisticated. In particular, most models have assumed instantaneous acceleration of the stellar winds. This has led to some discrepancies between the observed and predicted properties of some of these systems. For example, in close binary systems where this assumption becomes invalid, numerical models over-predict the resulting X-ray emission from the wind collision. Apart from the wind collision occurring within the wind acceleration zone, the radiative flux from the secondary star influences the acceleration of the stellar wind of the primary star, and vice versa (here and throughout this paper, the primary star is the star with the dominant wind). Stevens & Pollock (1994)

describe one aspect of this effect which they term ‘radiative inhibition’.

A far more severe interaction occurring for high-opacity winds was presented in a recent ground-breaking paper (Gayley, Owocki & Cranmer 1997). The effect, termed ‘sudden radiative braking’, occurs when the primary wind is suddenly decelerated by the radiative momentum flux that it encounters as it approaches the secondary. The strength of the wind collision may be substantially reduced, with lower pre-shock velocities and hence post-shock temperatures. The bow-shock geometry may also be significantly affected, and in extreme cases the shock may lift itself from the surface of the companion star where no normal ram-pressure balance would usually exist.

Incorporating the radiative driving of stellar winds into future numerical models will greatly enhance their predictive qualities. The ability to fit observational X-ray data to synthetic X-ray spectra from these models has already been demonstrated by Stevens et al. (1996). In this way fundamental stellar wind parameters such as

<sup>★</sup>E-mail: jmp@star.sr.bham.ac.uk

mass-loss rates and terminal velocities can be derived, and further development of the hydrodynamical models is expected to improve this process.

To date, numerical modellers have concentrated their efforts on systems with circular orbits. In such systems, the pre-shock velocity, and hence post-shock temperature, is constant in time. However, in binary systems with elliptical orbits, the wind collision between the stars may exhibit different features throughout the orbit. For example, in systems with unequal winds, the shocked region might be expected to collapse down on to the surface of the secondary star at periastron, whilst lifting off the secondary as it heads towards apastron. The importance of cooling is expected to vary with orbital separation, and the structure of the collision region might also be expected to be a function of whether the orbital separation is increasing or decreasing. Instabilities and the dynamics of the shocked flow may also be affected by a changing orbital separation.

In this paper we investigate the effect of a non-circular orbit on the wind collision. With the inclusion of radiative driving in our model, this becomes possible for the first time. Hydrodynamic simulations of the highly eccentric ( $e = 0.764$ ) Iota Orionis (HR 1889; HD 37043) system have been generated and are presented in the following sections. The dynamics of the wind collision are extensively discussed. A future paper on this system will present a detailed analysis of *ASCA* X-ray observations and the fits made to them by synthetic X-ray spectra generated from the hydrodynamical models. This should enable far tighter constraints on the mass-loss rates and terminal velocities of the stars in this system.

This paper is set out as follows. In Section 2, we present some theory of radiative driving, and in Section 3 we explain the details of the hydrodynamical calculations. Section 4 presents the results from the simulations performed. Section 5 summarizes and concludes.

## 2 DETAILS OF THE RADIATIVE DRIVING

As mentioned in Section 1, the assumed instantaneous acceleration of stellar winds to their observed terminal velocities has been a major shortcoming in past numerical models. This was recently overcome, however, in the paper by Gayley et al. (1997), in which the self-consistent inclusion of the radiative driving was a principal feature of their hydrodynamic code. The hydrodynamic results presented in this paper also incorporate this feature, allowing us to make a realistic study of the colliding wind properties in an eccentric system. Our inclusion of radiative driving is in many ways similar to that of Gayley et al., and we highlight the main points below.

The radiative acceleration of an early-type stellar wind arises from the scattering of stellar radiation in a large ensemble of spectral lines. Our calculation of these line acceleration terms is based on the standard CAK formalism developed for single OB-star winds (Castor, Abbott & Klein 1975), following the local Sobolev (1960) treatment of the line transport.

The total radiative force per unit mass owing to an ensemble of spectral lines is

$$f_{\text{rad}} = \frac{\sigma_e F}{c} M(t) K, \quad (1)$$

where  $\sigma_e$  is the mass scattering coefficient of free electrons ( $\sim 0.4 \text{ cm}^2 \text{ g}^{-1}$ ),  $F$  is the total flux,  $M(t)$  is the force multiplier function which expresses the effect of all lines, and  $K$  is the finite disc correction factor (FDCF). The first factor,  $\sigma_e F/c$ , is the force

arising from continuous absorption. The depth parameter,  $t$ , describes the optical depth in an expanding atmosphere. It is independent of line strength and is defined as

$$t = \sigma_e \rho v_{\text{th}} \left| \frac{dv}{dr} \right|^{-1}. \quad (2)$$

The definition of  $v_{\text{th}}$  is arbitrary, but following Abbott (1982) it is defined here as the thermal velocity of the hydrogen ion,

$$v_{\text{th}} = \left( \frac{2kT_{\text{eff}}}{m_{\text{H}}} \right)^{1/2}. \quad (3)$$

CAK found that the force multiplier factor varied approximately as a power of the depth parameter, such that it could be fitted with the formula

$$M(t) = kt^{-\alpha}. \quad (4)$$

$k$  represents the total number of lines present and  $\alpha$  represents the ratio of weak to strong lines. An optically thick line has  $\alpha = 1$ , while an optically thin one has  $\alpha = 0$ . Following the notation of Pauldrach, Puls & Kudritzki (1986),

$$\begin{aligned} w &= \frac{1}{2} v^2, \\ w' &= dw/du, \\ u &= -1/r, \end{aligned} \quad (5)$$

the finite disc correction factor can be defined as

$$K = \frac{[1 - (1 - R_*^2 u^2 - 2R_*^2 w u/w')^{\alpha+1}]}{[(\alpha + 1)R_*^2 u^2 (1 + 2w/w')]} \quad (6)$$

for  $r > R_*$ .

The above ‘MCAK’ formalism assumes single scattering. It is thus able to represent O-star winds and Wolf–Rayet (WR) winds which do not exceed the single-scattering limit. More powerful WR winds cannot be represented in this way. The use of the Sobolev approximation implies that the length-scale characterizing the velocity gradient exceeds the length-scale characterizing the ion distribution. Velocity gradient non-monotonicity (Lucy 1983; Puls, Owocki & Fullerton 1993), small-scale structure arising from the line-driven flow instability (Owocki 1994) and multiline scattering (Puls 1987; Lucy & Abbott 1993) all require a non-local line transport, and are not explicitly taken into account. The CAK line force parameters,  $\alpha$  and  $k$ , are fixed and assumed spatially constant.

The value of  $f_{\text{rad}}$  was computed over a solid angle covering the stellar disc using five sample points which were numerically integrated with Bode’s rule. An FDCF dynamically consistent with the actual local velocity gradient was used, which is a very subtle but important point mentioned by Gayley et al.

Some differences between the implementations of radiative driving in Gayley et al. and in this paper are as follows.

(i) In this paper both stars are included on the hydrodynamic grid. This has the advantage that radiative inhibition of both winds can occur. Although Gayley et al. did not include the WR star on their grid, radiative inhibition is likely to be totally negligible in their model, and indeed is also negligible in our model throughout most of its orbit.

(ii) Gayley et al. fix the CAK line force parameters to the wind material. On account of the vast difference in composition between WR winds and O-star winds, this seems entirely justified. In contrast, we fix the parameters to the radiation fields because we feel that for Iota Orionis the compositions of each wind should be fairly similar, whilst the temperature difference between the two stars results in radiation fields with very different flux distributions.

Ideally four sets of CAK line force parameters are needed: to describe the interaction of the primary radiation field with the primary and secondary winds, and of the secondary radiation field with the primary and secondary winds. However, it is not clear how the value of these four sets could be easily determined.

### 3 THE NUMERICAL MODEL

The numerical simulations presented in this paper were performed using *vH-1* (Blondin et al. 1990). This is a Lagrangian-remap version of the piecewise parabolic method (PPM), a third-order accurate finite difference scheme developed by Colella & Woodward (1984). The stellar winds are modelled as ideal gases with adiabatic index  $\gamma = 5/3$ . Radiative cooling is included via the method of operator splitting. The cooling rate was assumed to be that of an optically thin, solar-abundance plasma in ionization equilibrium. The cooling curve for the temperature range  $4.0 < \log T < 8.6$  was generated using the Raymond–Smith plasma code (Raymond & Smith 1977).

Previous studies of colliding wind systems using *vH-1* have been presented by Stevens et al. (1992, 1996), and Pittard & Stevens (1997). Most of the simulations presented in this paper were run on a medium-resolution two-dimensional grid with  $620 \times 200$  zones. One high-resolution simulation was also run on a grid of  $1000 \times 150$  zones. All of the zones were constant in size. Although binary rotation necessitates a full three-dimensional grid, a much less computationally expensive approximation was made. A cylindrically symmetric grid was used, with the symmetry axis ( $r$ -axis) concurrent with the vector between the centres of both stars, and the  $z$ -axis perpendicular to this. Although the axisymmetry will in fact be destroyed by the Coriolis force of the orbiting stellar system, the deviation is only pronounced for close binary systems and slow stellar winds. For the simulations in this paper, the final wind velocity is typically an order of magnitude larger than the orbital velocity, and orbital motion can be safely ignored. Only at periastron, where the position angle of the orbit changes the fastest, does this approximation begin to become troublesome.

The separation between the stars, and hence the location of the secondary star on the grid, was recalculated every time-step to account for the orbital motion. Zero-gradient boundary conditions were employed at the outer edge of the grid in order to allow mass to flow freely off it. Reflecting boundary conditions were employed on the symmetry axis along the line of centres of the stars.

The question of what boundary conditions to use at the stellar surfaces was more problematic. For the line force to be accurately calculated, the velocity and density gradients must be properly resolved. Near the surface of a star, the density of the wind can drop 4 orders of magnitude in  $\Delta r/R = 0.031$ , where  $R$  is the radius of the star. This resolution is unfeasible with our current implementation, so a method had to be found to initiate the stellar winds accurately. The best solution discovered was to map the initial acceleration of the wind on to the grid at the start of every time-step. This was done using an annulus of width 2 zones around each star. Although this is not a perfect solution (radiative inhibition cannot occur in this annulus, and it affects the orbital separation at which a collapsed shock detaches – see Section 4.3.3), it was found to be good enough in most cases.

The stellar winds were generated by first solving the relevant one-dimensional equations of motion as detailed by CAK. Once the stellar parameters ( $M_*$ ,  $R_*$ ,  $T_{\text{eff}}$ ) were chosen, the line force parameters,  $\alpha$  and  $k$ , were adjusted until the desired values of  $\dot{M}$  and  $v_\infty$  were obtained. The resultant density and velocity structures were

mapped on to the grid as the initial conditions, with the wind collision equidistant from the centres of both stars. At each evolution step the combined gravitational and radiative forces were calculated on each cell. The shadowing of cells from the radiative force of the primary by the secondary star was also included, and the orbital motion along the line of centres of the secondary relative to the primary was added to the remapping of the initial secondary wind. The material in cells with temperatures above  $10^6$  K was assumed to be completely ionized and hence totally transparent to the line photons responsible for the radiative driving. Such cells experience no net radiative force, although they are still affected by gravity.

#### 3.1 The Iota Orionis system

Iota Orionis (HR 1889; HD 37043) is a highly eccentric ( $e = 0.764$ ) O9 III + B1 III, double-lined spectroscopic binary which has been extensively observed throughout this century (e.g. Plaskett & Harper 1908, 1909; Miczaika 1951; Pearce 1953; Stickland et al. 1987). Despite problems associated with small velocity separations throughout a large proportion of the orbit (Hilditch et al. 1991), the orbital parameters are very well determined. Stickland et al. determined the period as 29.133 76 d, and presented a solution to the observed apsidal motion. The determination of the stellar parameters was helped enormously by a grazing eclipse which fixed the orbital inclination and the stellar masses to a small range.

As a consequence of the high eccentricity and moderately short period, there is a relatively close encounter between the two stars at periastron. The possibility of an enhanced, focused wind has recently led to renewed interest in this system (Stevens 1988; Gies, Wiggs & Bagnuolo 1993; Gies et al. 1996). Data consistent with this effect are presented in these papers, but at this stage the evidence remains inconclusive. It is certain, however, that at the least there will be some tidal deformation of the stars during the periastron passage.

Although the orbital and stellar parameters are well constrained, the mass-loss rates of the stars are, as usual, poorly known. The observationally determined mass-loss rates in the literature range from  $\dot{M}_{\text{radio}} = 3.2 \times 10^{-6} M_\odot \text{ yr}^{-1}$  to  $M_{\text{H}\alpha} = 1.0 \times 10^{-6} M_\odot \text{ yr}^{-1}$  (Lamers & Leitherer 1993), with many other estimations in between (e.g. de Jager, Nieuwenhuijzen & van der Hucht 1988; Leitherer 1988; Howarth & Prinja 1989). Another problem is the lack of knowledge of the mass-loss rate of the secondary star. The previous distance estimate of 450 pc was also checked against newly released results from *Hipparcos*. The parallax was found to be  $2.46 \pm 0.77$  mas, which translates into a distance of  $406_{-97}^{+105}$  pc. As expected, the original distance was confirmed to within the observational uncertainty of *Hipparcos*. The difference between the distances translates into a decrease of  $\dot{M}_{\text{radio}}$  by 17 per cent if the *Hipparcos* distance is correct. This is well within the standard assumption of a factor of 2 uncertainty in the radio determination and hence is not significant at this time.

From this wealth of information, two separate simulations with different mass-loss rates and wind momentum ratios were run with the aim of trying to cover the range in values listed above. The terminal velocities for both stars were chosen to represent average values from the literature. The parameters for the models are given in Table 1. Model cw\_1 is our best guess at this system, whilst the parameters of model cw\_2 have been chosen to give a more extreme momentum ratio between the two winds. Owing to the different masses assumed for the stars in model cw\_2, the calculated orbit is slightly different, although the eccentricity and period are the same.

**Table 1.** Simulation parameters.

Parameter	cw1	cw2
Mass of primary, $M_1 (M_\odot)$	38.9	30.0
Mass of secondary, $M_2 (M_\odot)$	18.9	14.8
Radius of primary, $R_1 (R_\odot)$	18.0	15.8
Radius of secondary, $R_2 (R_\odot)$	9.60	10.6
Effective temp. of primary, $T_1 (10^3 \text{ K})$	32.0	32.0
Effective temp. of secondary, $T_2 (10^3 \text{ K})$	21.0	21.0
$\dot{M}$ of primary ( $10^{-8} M_\odot \text{ yr}^{-1}$ )	61.6	30.6
$\dot{M}$ of secondary ( $10^{-8} M_\odot \text{ yr}^{-1}$ )	1.88	0.51
$v_\infty$ of primary ( $10^3 \text{ km s}^{-1}$ )	2.30	2.38
$v_\infty$ of secondary ( $10^3 \text{ km s}^{-1}$ )	2.20	1.99
Line force parameter, $\alpha_1$	0.59	0.60
Line force parameter, $\alpha_2$	0.565	0.565
Line force parameter, $k_1$	0.13	0.10
Line force parameter, $k_2$	0.30	0.11
Orbital period, $P$ (d)	29.13	29.13
Eccentricity, $e$	0.764	0.764
Periastron distance, $P_p (R_\odot)$	36.3	33.4
Apastron distance, $P_A (R_\odot)$	271.6	249.5

Model cw\_2 also favours dynamical effects such as radiative inhibition (Stevens & Pollock 1994) and sudden radiative braking (Gayley et al. 1997). Both effects are discussed in the next section.

## 4 SIMULATION RESULTS

### 4.1 Overview of the dynamics of model cw\_1

Fig. 1 shows 10 frames in a time-sequence of the density structure in the cw\_1 model. The stars are represented by black circles. Various numerical values from this simulation are listed in Table 2. Immediately apparent from Fig. 1 is that the colliding wind shock collapses on to the surface of the secondary star around periastron, but is eventually pushed off as the secondary heads towards apastron. At periastron, the momentum flux of the primary's wind totally overwhelms that of the secondary's, and the shock is pinned very firmly. As the orbital separation increases, the relative momentum fluxes become less imbalanced, and the shock is pinned less firmly, before later becoming detached. At the same time the half-opening angle of the shock increases.

The post-shock wind of the primary is radiative at periastron, but quickly becomes adiabatic as the orbital separation (and hence the distance from the primary to the collision shock) increases. The secondary's wind is also adiabatic at apastron, but remains radiative for a longer duration around periastron than the primary's wind. This is because when the orbital separation is small the shocked region is collapsed on to, or is very close to, the surface of the secondary, and the post-shock density is consequently much higher. The mix of low- and high-density gas, together with the velocity shear along the contact discontinuity, produces very strong instabilities in the post-shock flow. As the shock struggles to lift itself off the surface of the secondary, it oscillates up and down and the cooling post-shock flow of the secondary forms 'fingers' into the adiabatic post-shock flow of the primary. These are believed to be thin-shell instabilities. At such times, the shocked secondary wind is bounded on one side by the hot post-shock gas of the primary wind, and on the other side by the nearly isothermal shock of the cooling secondary wind. As similarly noted by Stevens et al. (1992), this instability appears to progress by kinking the cooling shock to the point where these 'fingers' of dense gas are pushed from the

indented regions of the shock front into the hot gas of the adiabatic post-shock primary wind. These are subject to the action of the Kelvin–Helmholtz instability and are wound up by the vortices and eddies existing in the post-shock flow. These effects combined appear to 'shred' the secondary wind and the remnants are turbulently advected away.

As the secondary star passes apastron and begins to re-approach the primary, the shock again collapses on to its surface. The orbital separation at which this occurs is approximately the same as when the shock detached itself. However, the nature of the post-shock flow is substantially different in the second half of the orbit from that in the first half. The half-opening angle is reduced and the oscillations of the shock on the surface of the secondary are more violent, leading to more structure later in the flow. The difference in the half-opening angle is entirely due to the change in relative velocity between the stellar wind of the primary and the orbital velocity of the secondary. In the first half of the simulation, as the secondary heads towards apastron, this relative velocity is less than that occurring in the second half, when the secondary is heading towards periastron. The secondary also has to 'punch' through a larger mass-column of the primary wind in the second half, explaining why the primary's wind is also more strongly cooling. When both primary and secondary post-shock flows become strongly cooling, the shocked region is compressed into a thin sheet. This oscillates slightly, but as a whole the post-shock flow is much smoother and more stable than at any other point in the orbit. The half-opening angle increases at periastron as the orbital separation stops decreasing. As the secondary once again begins to draw away from the primary, it increases still further and the shocked flow again becomes unstable.

### 4.2 Overview of the dynamics of model cw\_2

The density structure in the cw\_2 model is shown as a time-sequence in Fig. 2. Various numerical values from this simulation are again listed in Table 2. The most obvious difference of the cw\_2 simulation is that the shock does not detach from the surface of the secondary, even when it is at apastron. This is due to the higher wind momentum ratio in this model, which also leads to a smaller value for the shock half-opening angle throughout the entire orbit. As the secondary passes apastron, a high-density, low-temperature structure forms along the contact discontinuity, which is bounded on both sides by lower density, higher temperature components. Just before periastron the post-shock structure changes again, first into four components, and then back into three components. In almost all other areas, however, the dynamics of the two models are very similar. Instabilities are again ubiquitous in the flow, and the post-shock gas again contains a substantial amount of structure.

The final frame in Fig. 2 shows a shock moving away from the secondary star into its own unshocked wind. This is simply a numerical effect caused by the motion of the secondary star on the grid changing by  $\sim 500 \text{ km s}^{-1}$  in a short period of time as it moves through periastron. When this difference is applied to the remapping of the initial acceleration of the secondary wind, it results in a fast wind, emitted later, ramming into a slower, previously emitted wind. This effect would not occur in three-dimensional models which would be much more suitable for investigating the shock structure at periastron. However, the temperature of the shock is low and does not affect our calculation of the intrinsic X-ray emission in Section 4.5. Hence the effect is merely cosmetic. A similar, although less visible, artefact also occurs in the cw\_1 model.

### 4.3 Wind velocity structure

Two possible effects which alter the wind velocity structure in early-type binary systems have already been mentioned in Section 1. Stevens & Pollock (1994) performed one-dimensional numerical calculations along the line of centres of various model binary systems to investigate the effect of the presence of a companion star. They found that the wind acceleration towards the stagnation point was inhibited because the resultant radiation force was smaller than for a single star. This effect was termed ‘radiative inhibition’. For their model of Iota Orionis, the pre-shock velocity of the primary wind was found hardly to differ from the single-star value when the system was at apastron, but at periastron the respective values differed by about a factor of 2. With the inclusion of the countervailing influence of the companion’s gravitational attraction, inequalities governing the stellar mass-loss flux were also derived. The stagnation mass-loss rate was found to increase at periastron by about 25 per cent.

The second and more severe effect was discovered by Gayley et al. (1997): the primary wind may be suddenly decelerated by the radiative momentum flux that it encounters as it approaches the secondary. This was termed ‘sudden radiative braking’, and is believed to be most important in systems where the secondary is the more luminous star (e.g. WR+O systems). In their paper, detailed two-dimensional hydrodynamical simulations were made of the wind collision in the WR+O binary V444 Cygni and compared with a one-dimensional analytical analysis. The results agreed well and the analytic theory was applied to 14 additional hot-star binary systems, amongst them Iota Orionis. Sudden radiative braking was found to be particularly interesting in this system, because its orbital eccentricity and wind momentum ratio are believed to be at just the correct values to take it from one side of their homology diagram (their fig. 5) to the other. As such, it passes through the region where radiative braking only plays a small role, the position where no ‘normal’ ram balance occurs and radiative braking becomes important, and the point when this effect can no longer stop the shock collapsing on to the surface of the secondary and photospheric collision occurs.

Our numerical simulations combine the two discoveries above into a model in which both effects can be studied together, and hence comprise a further breakthrough in the correct dynamical modelling of colliding wind systems. Each of these effects with regard to our simulations is now discussed in turn.

#### 4.3.1 Radiative inhibition

The effect of radiative inhibition in our models can be seen in Fig. 3. At apastron, as Stevens & Pollock predicted, there is hardly any difference between the pre-shock value of the primary wind and the single-star value. However, in contrast to their prediction at periastron, we again find very little radiative inhibition. The discrepancy in this latter result is attributed to differences in the codes used in both papers. In particular,

- (i) their stellar parameters favour radiative inhibition more than ours do (e.g. their luminosity ratio  $L_1/L_2 = 13$ , whilst ours is 19);
- (ii) they use only a single force multiplier for both winds ( $\alpha = 0.59$ ,  $k = 0.17$ );
- (iii) their FDCF is only radially dependent, and is not dependent on  $v$  or  $dv/dr$ .

It is not entirely certain what exact effect points (ii) and (iii) have on

the solution, although it is reasonable to assume that they account for at least some of the differences that we see.

With regard to mass-loss rates in our simulations, an increase was seen along the line of centres in the primary wind at periastron, but the effect was very small at only 1.7 per cent. This is much lower than the  $\sim 25$  per cent increase predicted by Stevens & Pollock. We note, however, that owing to the implementation of our boundary conditions at the stellar surfaces, a change in the stagnation mass-loss rate would not be expected. This is because the mass-loss rates in the CAK formalism are fixed at the critical point, which lies very close to the photosphere and within our annulus. Hence it seems likely that our witnessed change is only a small temporal effect linked to a changing velocity field, and in this respect the calculations of Stevens & Pollock are superior.

This leads to another possible explanation for the differences in the degree of radiative inhibition between the two sets of results. Additional simulations performed suggest that for a given net radiative force the product  $Mv_\infty$  is constant, so if  $M$  increases,  $v_\infty$  decreases. Thus the greater part of the radiative inhibition in the calculations of Stevens & Pollock may in fact be due to the primary star struggling to accelerate a more massive wind, and not due to the radiation field of the secondary *per se*, as originally thought. This clearly warrants further investigation beyond the scope of this paper.

#### 4.3.2 Sudden radiative braking

Sudden radiative braking occurs in model cw\_1 when the shock collapses on to the surface of the secondary. The velocity profile along the line of centres of frame 2 in Fig. 1 is shown in Fig. 4. The pre-shock velocity is indicated with an arrow. From Table 2 we see that the maximum reduction in the pre-shock velocity is  $\sim 25$  per cent. Because the post-shock gas temperature is given by  $kT_s \sim 1.2 v_8^2$  keV for material of solar abundance, where  $v_8$  is the pre-shock velocity in units of  $10^8$  cm s $^{-1}$ , this results in a reduction in the temperature of  $\sim 50$  per cent.

Fig. 5 demonstrates the level of agreement between our numerical results (solid line) and the analytic theory (dotted line) derived in Gayley et al.’s paper. The velocity solution from frame 8 of Fig. 1 is shown. The maximum velocity obtained by the primary wind in our simulation was used to scale the results of their equation (16). The pre-shock velocity is again indicated with an arrow. Immediately apparent is that the velocity of the primary wind in our numerical simulation continues to increase past the point where the analytical solution first starts to show it being braked. This can be attributed to the radiation force from the primary star, which is not included in the simplified analytical theory. However, once the onset of braking is reached, it is even more sudden in our numerical simulations.

These differences are in exact agreement with those reported in Gayley et al.’s paper: they also found a delay in the onset of braking which then became more sudden than indicated by their analytic theory. They attributed this to their inclusion of the secondary gravitational field in their numerical model, which can be understood as follows. The radiation and gravitational fields of the secondary create two opposite forces on the primary wind. Consider first the radiation field: as it deposits momentum into the oncoming primary wind and begins to decelerate it, the velocity gradient increases and hence the momentum that can be deposited increases, so that the wind may be braked very quickly. However, when we consider the gravitational field as well, it becomes obvious that this reduces the deceleration of the primary wind. It is thought that this

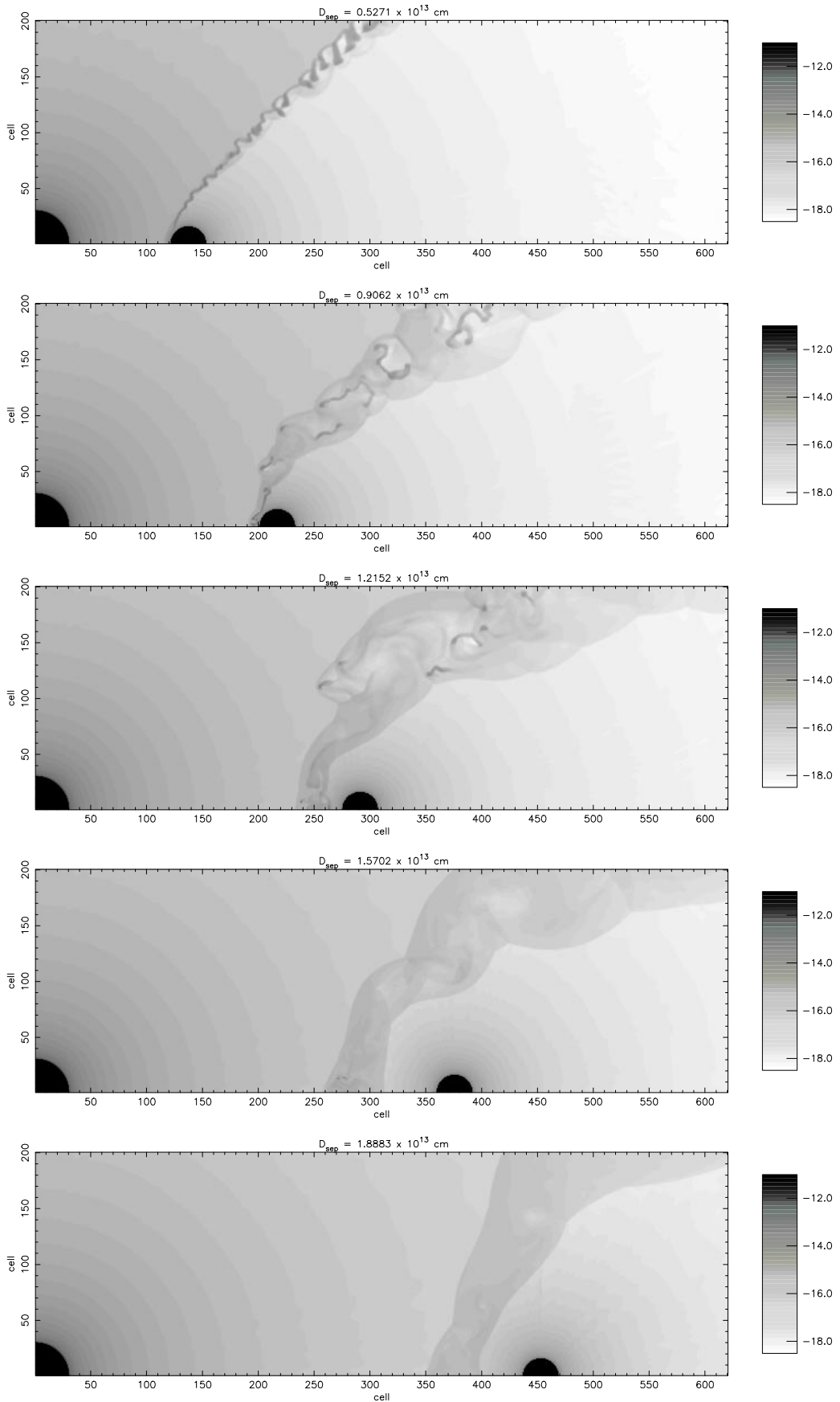


**Figure 1.** Log density plots ( $\text{g cm}^{-3}$ ) of model cw\_1.

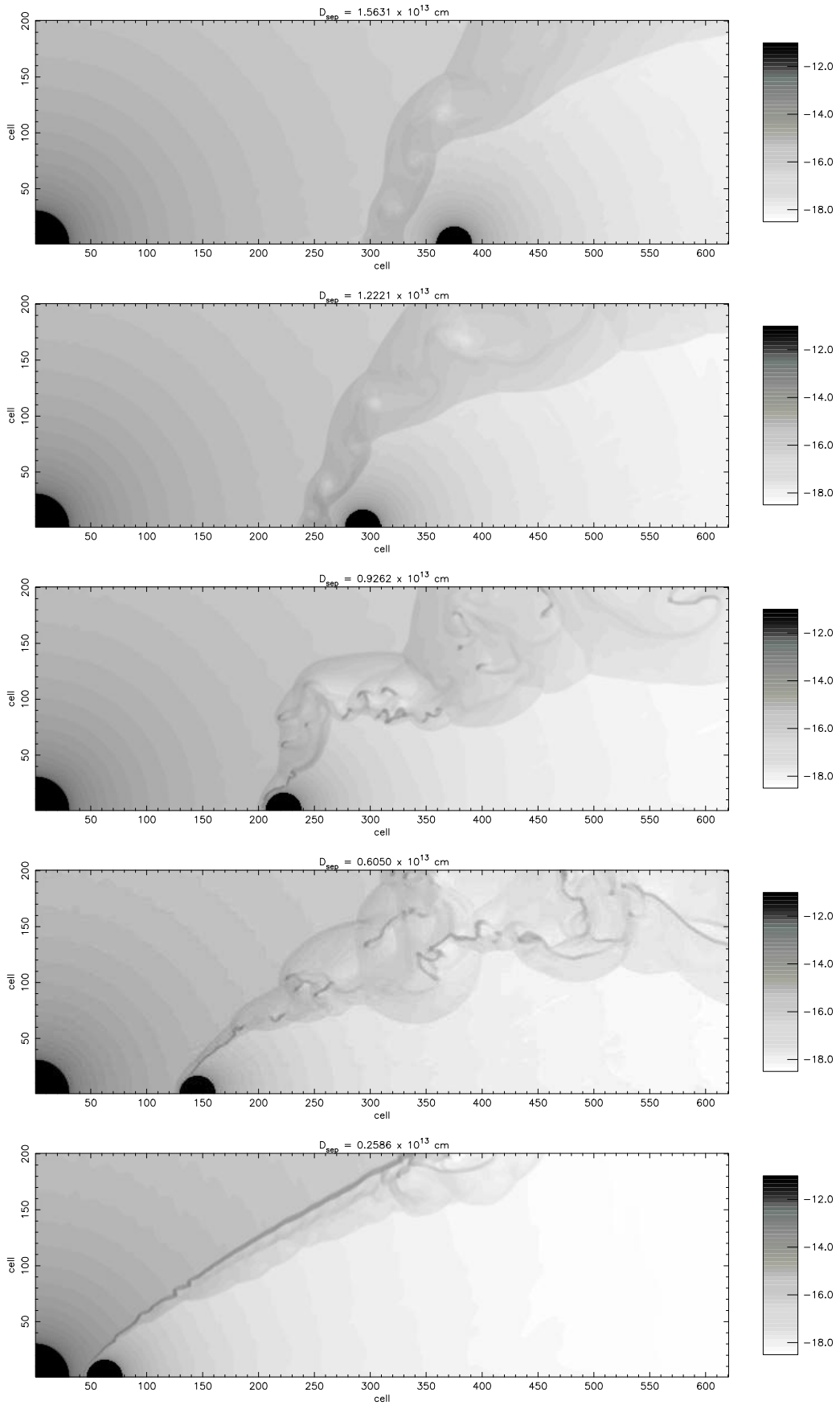
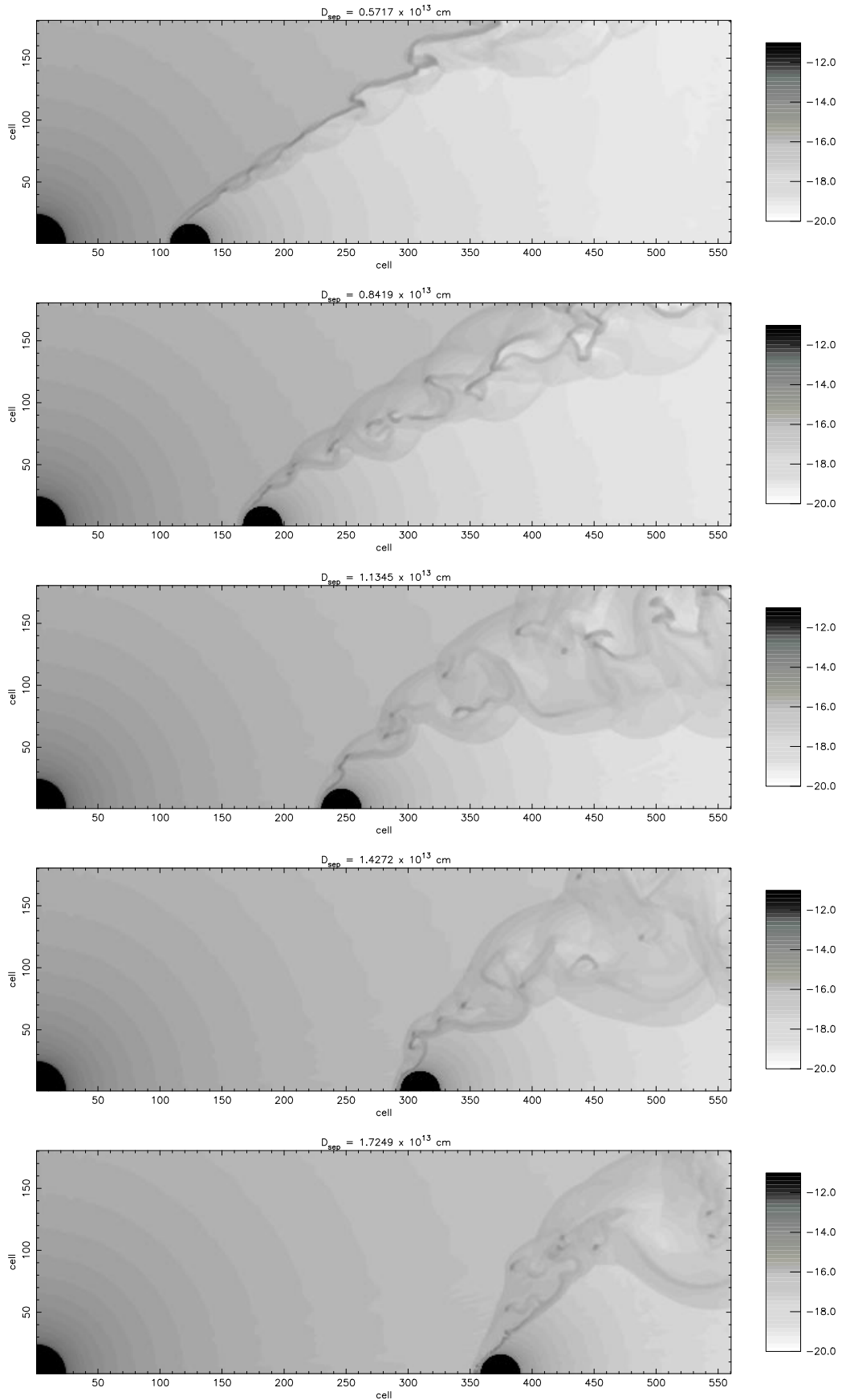


Figure 1 – continued



**Figure 2.** Log density plots ( $\text{g cm}^{-3}$ ) of model cw\_2.

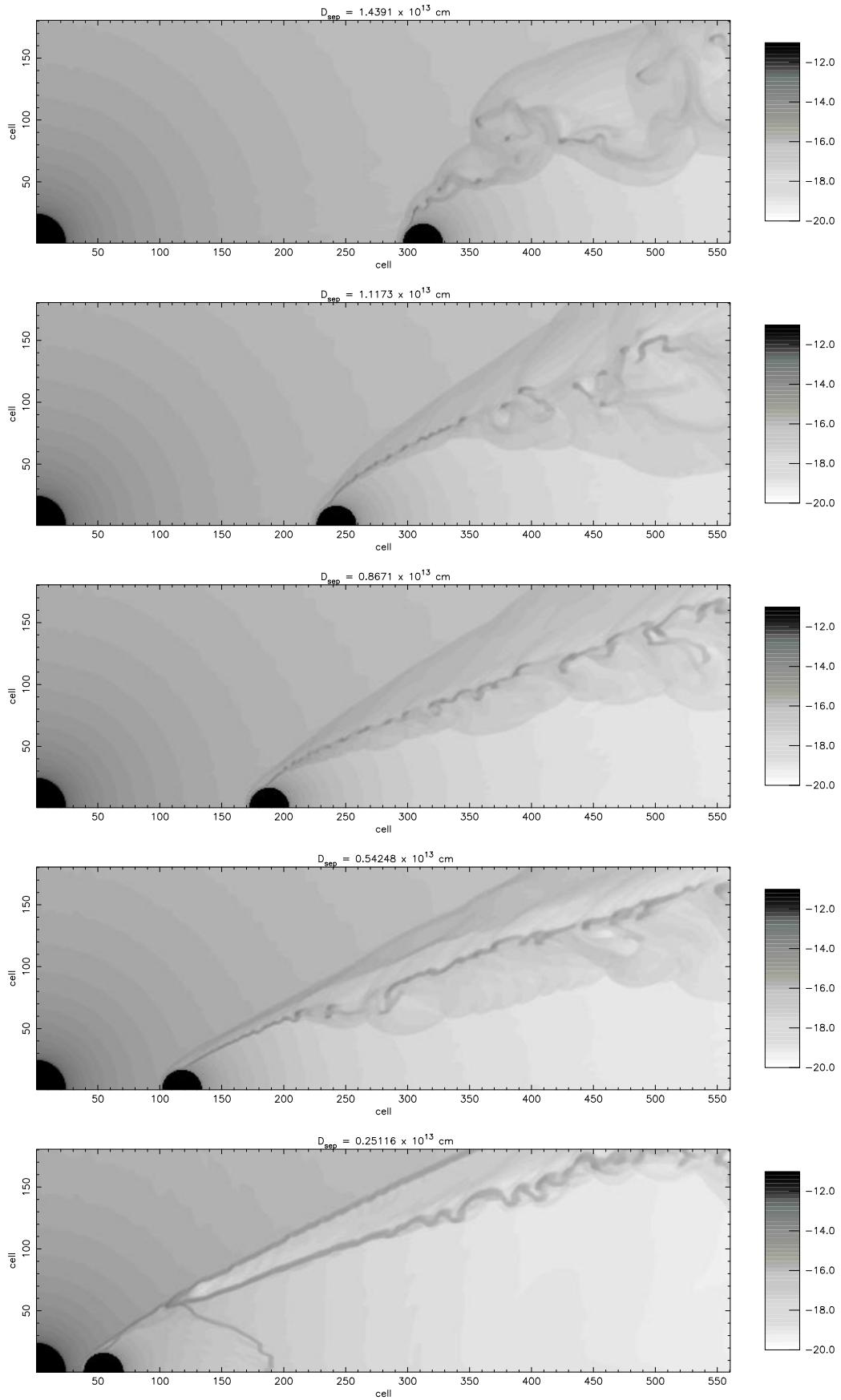
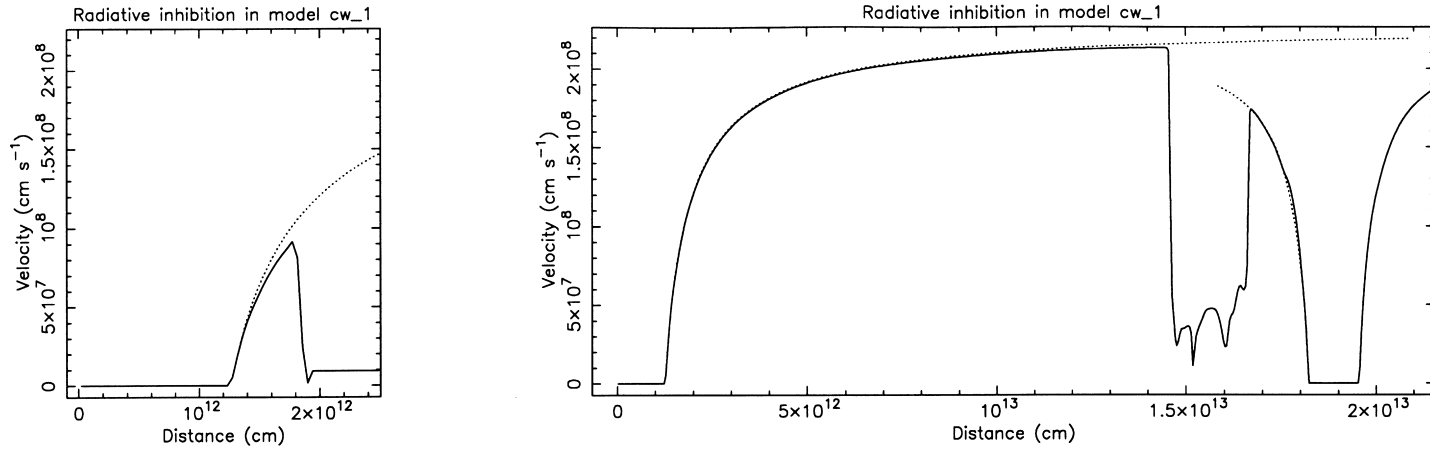


Figure 2 – continued

**Table 2.** Results of models cw1 and cw2. The separation distance, time since periastron, phase, maximum velocity of the primary wind along the line of centres, pre-shock velocity of the primary wind along the line of centres, whether there is any radiative braking, and maximum post-shock temperature on the grid are shown for each model for the frames in Figs 1 and 2.

Model cw_1										
$D_{\text{sep}}$ ( $10^{13}$ cm)	0.5721	0.9062	1.2152	1.5702	1.8883	1.5631	1.2221	0.9262	0.6050	0.2586
time ( $10^6$ s)	0.1238	0.2473	0.3979	0.6462	1.2573	1.8708	2.1113	2.2574	2.3792	2.5249
Phase	0.049	0.098	0.158	0.257	0.499	0.743	0.839	0.897	0.945	0.003
$v_{\text{max}}$ before shock ( $10^8$ cm s $^{-1}$ )	1.76	1.96	2.05	2.09	2.13	2.10	2.06	1.98	1.81	0.91
$v$ at shock ( $10^8$ cm s $^{-1}$ )	1.68	1.58	2.03	2.08	2.13	2.10	2.04	1.65	1.63	0.91
Radiative braking?	yes	yes	slight	slight	no	no	slight	yes	yes	no
$T_{\text{max}}$ ( $10^7$ K)	2.34	3.30	5.83	6.87	8.97	7.26	6.44	5.69	5.36	1.02
Model cw_2										
$D_{\text{sep}}$ ( $10^{13}$ cm)	0.5717	0.8419	1.1345	1.4272	1.7249	1.4391	1.1173	0.8671	0.5425	0.2512
time ( $10^6$ s)	0.1428	0.2575	0.4185	0.6481	1.2591	1.8694	2.1218	2.2597	2.3976	2.5352
Phase	0.057	0.102	0.166	0.257	0.500	0.743	0.843	0.898	0.953	0.007
$v_{\text{max}}$ before shock ( $10^8$ cm s $^{-1}$ )	2.10	2.28	2.37	2.42	2.46	2.42	2.37	2.29	2.08	1.04
$v$ at shock ( $10^8$ cm s $^{-1}$ )	2.01	2.05	2.03	1.97	1.96	1.99	2.01	2.02	2.04	1.04
Radiative braking?	yes	yes	yes	yes	yes	yes	yes	yes	yes	no
$T_{\text{max}}$ ( $10^7$ K)	3.74	4.90	5.57	5.92	6.46	6.52	7.36	8.06	6.70	2.00



**Figure 3.** Radiative inhibition in model cw\_1 at periastron (left) and apastron (right). The solid line shows the numerical result and the dotted line shows the single-star solution. A small amount of radiative inhibition occurs at periastron, when the radiation field of the secondary star has some influence on the acceleration of the primary wind towards the stagnation point. At apastron the stars are too widely separated for there to be any significant effect.

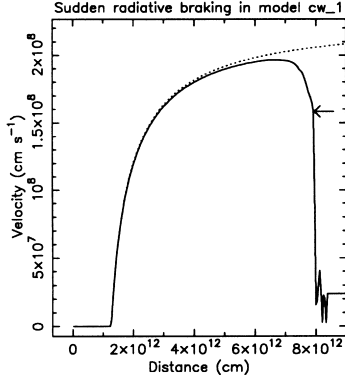


**Figure 4.** Sudden radiative braking in frame 2 of model cw1. The solid line indicates the velocity profile along the line of centres. The arrow marks the position where the primary wind collides with the shock, and clearly indicates a reduction in the pre-shock velocity of  $\sim 25$  per cent. The dotted line shows the single-star velocity solution and indicates the degree of radiative inhibition.

‘competition’ initially delays the onset of radiative braking. When it is overcome, the braking is then more severe as a result of the unbraked wind being closer to the secondary than would otherwise have been the case. The assumption in the analytic theory that the braking occurs in the limit of a plane-parallel layer close to the secondary, and thus that the FDCF has a value equal to  $1/(1 + \alpha)$ , may also account for some of the difference.

The analytical theory in Gayley et al. can also be applied to determine the orbital separation,  $D_b$ , at which the braking radius,  $x_b$ , is equal to the photospheric radius of the secondary. Once the orbital separation exceeds  $D_b$ , the shock should lift off the secondary’s surface. Putting the values for model cw\_1 into Gayley et al.’s equation (18) gives  $D_b = 9.55 \times 10^{12}$  cm. Comparing this with our simulations, we see from Fig. 1 that the shock detaches between the second and third frames, at an orbital separation between  $0.906 \times 10^{13}$  and  $1.215 \times 10^{13}$  cm. Thus, despite the previously mentioned discrepancies between the numerical and analytical results, it appears that on this issue they agree quite well.

#### 4.3.3 High-resolution results

To provide a detailed look at the hydrodynamics of the shock detachment, a further simulation using the same parameters as

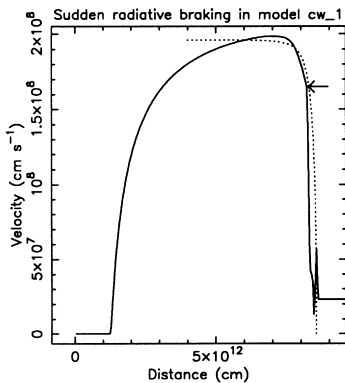


**Figure 5.** Sudden radiative braking in frame 8 of model cw1. The solid line indicates the velocity profile along the line of centres. The arrow marks the position where the primary wind collides with the shock. The dotted line shows the result from the simplified analytical solution of Gayley et al.

model cw\_1 was run on a high-resolution grid of  $1000 \times 150$  zones. This enabled the secondary star to be doubled from 16 to 32 zones in radius, and the remapping of its wind to be decreased from  $1.125R_2$  to  $1.0625R_2$ . This lowers the average remapped velocity from 355 to  $200 \text{ km s}^{-1}$ .

It was quickly discovered that, despite the apparent agreement in Section 4.3.2, the orbital separation at the point where the shock detaches itself is dependent on the extent of the remapping around the secondary star. The reduction in radius of the remapping reduces the momentum flux that the secondary wind automatically has, and hence makes it harder for it to overcome the ram pressure that the primary wind imparts to the shock as it pins it to the surface of the secondary.

Because of the orbital motion and the oscillation of the shock, it was very difficult to tell exactly when the shock started to detach. Close examination of the flow showed that the shock lifted itself off the surface a number of times before quickly crashing down again. Once it was lifted past a certain point, however, the secondary wind established itself permanently, and the shock was rapidly driven away from the surface. In the high-resolution simulation this appeared to occur when  $D_{\text{sep}}$  was approximately  $1.54 \times 10^{13}$  cm, a significantly greater value than previously found.

Although we have discovered that the value of  $D_b$  is currently resolution-dependent, the level of sudden radiative braking and radiative inhibition in the models is not. The onset and suddenness of the radiative braking are identical in both model cw\_1 and its higher resolution counterpart. Hence the dependence of  $D_b$  on resolution is more to do with the lower boundary condition than with anything else. Increasing the resolution still further may result in another value of  $D_b$ , although the simulations are expected eventually to become resolution-independent, as the decrease in the remapped wind momentum flux is balanced by an increase in the radiative momentum flux as the surface of the star is approached. Further modelling should resolve this issue. Until then, however, the X-ray light curves in Section 4.5 must be treated with some caution, because a different value of  $D_b$  alters the time at which the soft intrinsic emission suddenly decreases. Without being aware of this problem, inaccurate mass-loss rates may potentially be inferred.

#### 4.4 Post-shock temperatures

The maximum post-shock temperature in the orbit of model cw\_1 occurs, as expected, at apastron. This is when the pre-shock velocities of both the primary and secondary winds are highest, and when the post-shock flow is the most adiabatic. Hence, at apastron, the X-ray emission will be at its hardest. In contrast,  $T_{\text{max}}$  in model cw\_2 does not occur at apastron, instead occurring over 10 d later as the secondary star nears periastron. The difference between the models is due to the shock remaining collapsed on to the surface of the secondary and the differing amounts of radiative inhibition and sudden radiative braking that take place at various parts of the orbit. In model cw\_1, once the shock detaches from the surface of the secondary, sudden radiative braking becomes unimportant, leading to high pre-shock velocities around apastron. In model cw\_2, the shock never detaches from the surface of the secondary, so sudden radiative braking remains important even at apastron. Once model cw\_1 passes apastron and the shock recollapses on to the surface of the secondary, sudden radiative braking once again becomes important, keeping the pre-shock velocity down. In model cw\_2, however, neither the initial radiative inhibition nor the subsequent sudden radiative braking of the

primary's wind is as severe at this stage of the orbit, leading to a higher pre-shock velocity. Once this is combined with the orbital motion of the secondary star towards the primary, the relative shock velocity is higher, and the post-shock temperature reaches a maximum in frame 8 (frame 9 in Fig. 2 actually has the greatest relative shock velocity, but the wind collision occurs much closer to the primary star, with the effect that the post-shock density is higher, allowing the shock to cool more quickly).

#### 4.5 Intrinsic X-ray emission

In both models cw\_1 and cw\_2, the pre-shock velocity of the primary wind is significantly higher than that of the secondary when the shock is collapsed on to the photosphere. Hence the shocked primary wind emits most of the high-energy X-rays whilst the cooler secondary wind emits most of the low-energy X-rays. This is also true in model cw\_1 when the shock detaches, but to a lesser degree.

Intrinsic synthetic X-ray spectra generated from model cw\_1 are shown in Fig. 6. The change in the hardness of the emission throughout the orbit is immediately striking. The high-energy X-ray emission is strongly reduced around periastron. This is caused by the pre-shock velocity of the primary wind decreasing from  $\sim 2000$  to  $\sim 1000$  km s $^{-1}$ , as the secondary star moves deep into its acceleration zone. However, there is significant soft X-ray emission at this orbital phase, owing to the high densities and hence high cooling rate in the collapsed shock. At apastron, the post-shock flow is adiabatic so the X-ray emission below  $\sim 0.25$  keV is reduced. The high pre-shock velocities of both the primary and secondary winds at this phase, however, generate a significant amount of X-ray emission above 5 keV. Thus the intrinsic spectra are soft at periastron and hard at apastron. The intrinsic spectra at periastron change significantly over a short time-scale as the orbital separation between the stars quickly alters. In contrast, the intrinsic spectra at apastron are roughly constant for over a fortnight, until the shock begins to recollapse on to the secondary.

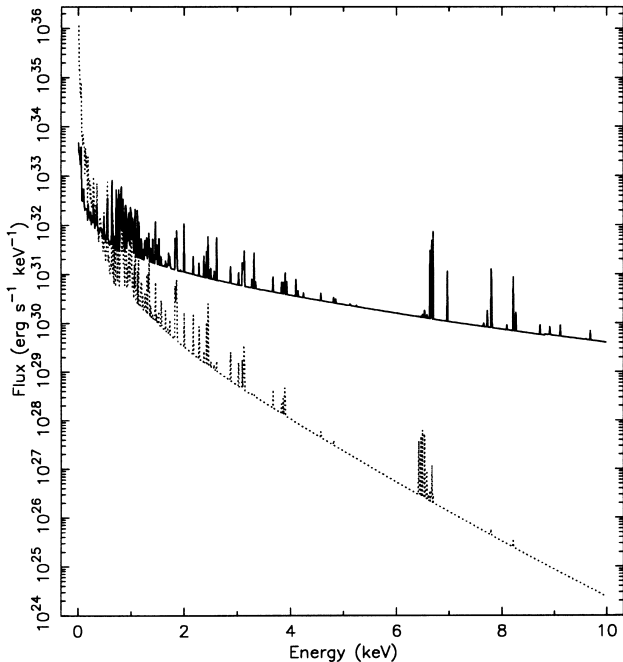


**Figure 6.** Intrinsic synthetic X-ray spectra generated from model cw\_1 at periastron (dotted) and apastron (solid).

Intrinsic X-ray light curves for models cw\_1 and cw\_2 are shown in Fig. 7. The solid line shows the variation for model cw\_1 on the  $620 \times 200$  grid ( $2.59 \times 10^{13}$  cm by  $8.35 \times 10^{12}$  cm) shown in Fig. 1. When the shock detaches from the secondary and the post-shock

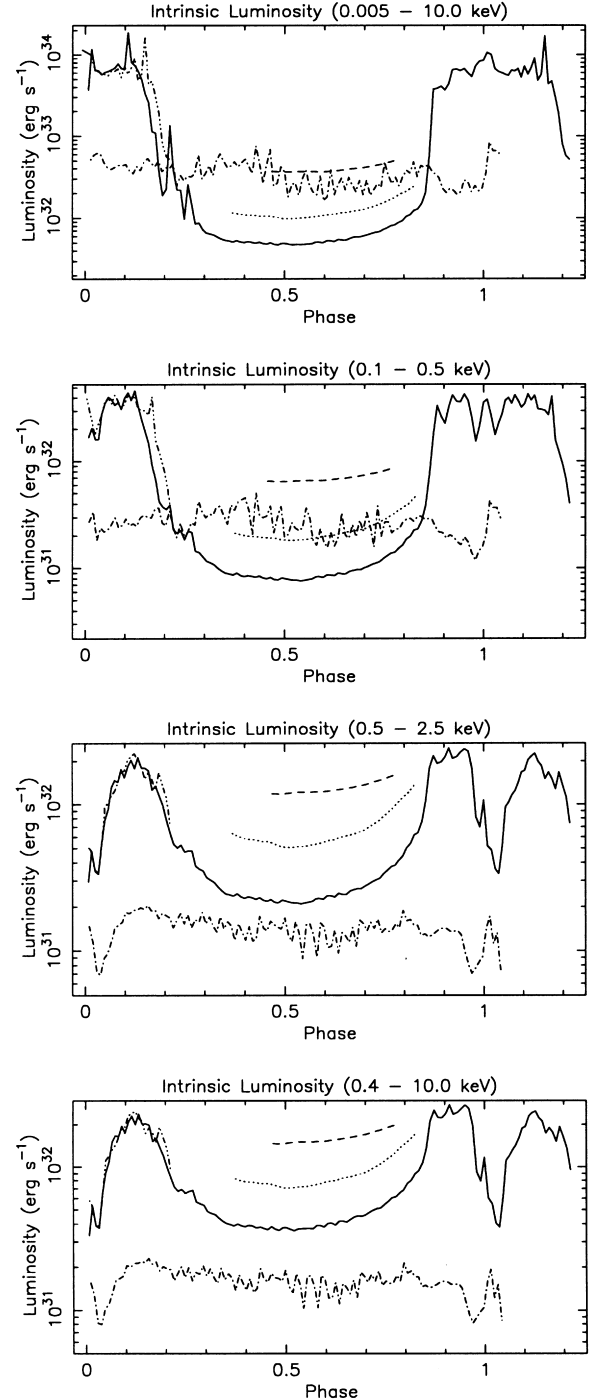


**Figure 7.** Intrinsic X-ray lightcurves of models cw\_1 and cw\_2. The solid line shows the variation with phase for model cw\_1 on the grid shown in Fig. 1. The dotted and short-dashed lines show the variation around apastron when the shock detaches, at which point bigger grids are needed to 'capture' all of the intrinsic emission. The latter grid successfully achieves this. The phase repeatability of the shock detachment is shown by the dash-triple-dotted curve. The intrinsic lightcurve from model cw\_2 is shown as the dash-dotted curve. It is characterized by almost constant X-ray emission in all four energy bands throughout the entire orbit.

flow becomes adiabatic, the X-ray emission drops dramatically. Concerns over whether all of the intrinsic emission was being ‘captured’ at this phase, however, led to its recalculation at apastron using bigger grids. The dotted line shows the emission using a grid of dimensions  $5.18 \times 10^{13}$  cm by  $1.67 \times 10^{13}$  cm, and the short-dashed line the emission from a grid of dimensions  $6.68 \times 10^{13}$  cm by  $6.68 \times 10^{13}$  cm. The latter grid was large enough to ‘capture’ all of the intrinsic emission. Thus we see that the soft intrinsic X-ray emission, which contributes most of the total emission, drops violently by over an order of magnitude as soon as the wind collision becomes adiabatic. In contrast, the higher energy emission remains roughly constant during this transition. The decrease of the high-energy emission around periastron is shown by the almost order-of-magnitude decrease in the *ASCA* energy band. This drop in emission lasts for approximately 2 d.

The phase repeatability of the X-ray light curve is shown with the second orbit superimposed on to the solid line of the first as the dash–triple-dotted curve. A small phase difference exists, caused by a slightly different time for the detachment of the shock from the surface of the secondary, but the agreement is very good.

The light curve of the cw\_2 model using the  $620 \times 200$  grid ( $2.59 \times 10^{13}$  cm by  $8.35 \times 10^{12}$  cm) shown in Fig. 2 is plotted as the dash–dotted line. It is immediately apparent that the different density and temperature structures between models cw\_1 and cw\_2 lead to a significantly different light curve, which in contrast to that from model cw\_1 is characterized by an almost constant X-ray emission in all four energy bands throughout the entire orbit. The only similarity is the decrease in the higher energy X-ray emission at periastron.

This difference is exceedingly significant because, if it were repeated in absorbed X-ray light curves, one would be able to distinguish between winds of different momentum ratios, and accurate values for the mass-loss rates could be assigned to each star. Owing to the observational uncertainties, this ability would be very important.

## 5 DISCUSSION

Our hydrodynamic models have shown the complexity of the colliding wind in Iota Orionis. The radiation fields of the two stars can significantly affect the wind dynamics, and both radiative inhibition and sudden radiative braking occur at various stages in the orbit. The imbalance of the wind momentum flux, coupled with the high eccentricity of the orbit, leads to some very interesting shock behaviour. In one of our models this results in the shock being pushed off the photosphere of the secondary. In both models instabilities are ubiquitous, leading to significant structure in the post-shock flow.

The hydrodynamical models can also be used to interpret the X-ray emission from Iota Orionis, most of which should be from the colliding wind shock. Observations with the *Einstein* X-ray observatory (Chlebowski, Harnden & Sciortino 1989) found a luminosity of  $3.0 \times 10^{32}$  erg s<sup>-1</sup> and a characteristic X-ray temperature of  $0.51 \pm 0.08$  keV, assuming an interstellar absorption column of  $0.2 \times 10^{21}$  cm<sup>-2</sup>. The latter was derived from an *IUE* value of  $N_{\text{H I}}$  (Shull & Van Steenberg 1985) and a *Copernicus* value of  $N_{\text{H II}}$  (Savage et al. 1977). Snow, Cash & Grady (1981) reported variable X-ray emission, although a subsequent re-analysis by Collura et al. (1989) resulted only in upper limits for any variability.

Our preliminary results suggest that a large reduction in the soft X-ray emission would take place if the shock detached from the surface of the secondary, whilst a dip in the hard X-ray emission

occurs at periastron. X-ray data from the *ASCA* satellite, taken at two orbital phases around periastron and apastron, are currently being analysed, and the results will be presented in a forthcoming paper.

The possibility of an enhanced, focused wind during the close encounter between the two stars at periastron has been the driving force behind recent observations of this system. Gies et al. (1993) confirm the earlier conclusion of Strickland et al. (1987) that there is no major change in the large-scale wind structure. However, their discovery of a slight excess in the blue wing of the H $\alpha$  line led to the tentative conclusion of enhanced mass loss in the immediate vicinity between the stars. To put this on a firmer footing, Gies et al. (1996) obtained further spectra of the H $\alpha$  and He I 6678-Å line profiles during a single periastron passage. Blueshifted emission was again seen, but the evidence for such an effect remains inconclusive, mainly because the interpretation is not unique. Tidal distortions of the primary could lead to profile variations near periastron, and Ebbets (1982) has demonstrated that many luminous O stars show randomly variable emission in the core of H $\alpha$ .

Despite this, numerical calculations (Stevens 1988; Stevens & Pollock 1994) suggest that an increase in the stagnation mass-loss rate should occur, although the effect may be relatively small ( $\sim 25$  per cent) and over a relatively short time-scale (a few hours). Unfortunately our hydrodynamical simulations cannot yet help in this matter because of our implementation of the initial acceleration of each wind, resulting in fixed mass-loss rates for both stars.

While these simulations have provided a new insight into the dynamics of the colliding wind in Iota Orionis, the limitation to two dimensions is a poor approximation at periastron. The behaviour of the shock whilst collapsed on to the secondary photosphere may be entirely different in three-dimensional models. Tidal deformation of the stars at periastron would also affect the post-shock flow to some degree, as would the inclusion of stellar rotation. The next stage in the development of our hydrodynamical models is to include some of these effects. A three-dimensional version of our code has already been implemented and we expect to present results shortly.

## ACKNOWLEDGMENTS

We thank Ian Stevens and Dave Strickland for discussions during this work. The numerical simulations were computed at the Birmingham Starlink node. Funding from the School of Physics and Astronomy is gratefully acknowledged. This research has made use of the SIMBAD astronomical data base at the CDS, Strasbourg.

## REFERENCES

- Abbott D.C., 1982, *ApJ*, 259, 282
- Blondin J.M., Kallman T.R., Fryxell B.A., Taam R.E., 1990, *ApJ*, 356, 591
- Castor J.I., Abbott D.C., Klein R.I., 1975, *ApJ*, 195, 157
- Chlebowski T., Harnden F.R., Jr, Sciortino S., 1989, *ApJ*, 341, 427
- Colella P., Woodward P.R., 1984, *J. Comput. Phys.*, 54, 174
- Collura A., Sciortino S., Serio S., Vaiana G.S., Harnden F.R., Jr, Rosner R., 1989, *ApJ*, 338, 296
- de Jager C., Nieuwenhuijzen H., van der Hucht K.A., 1988, *A&AS*, 72, 259
- Ebbets D., 1982, *ApJS*, 48, 399
- Gayley K.G., Owocki S.P., Cranmer S.R., 1997, *ApJ*, 475, 786
- Gies D.R., Wiggs M.S., Bagnuolo W.G., Jr, 1993, *ApJ*, 403, 752
- Gies D.R., Barry D.J., Bagnuolo W.G., Jr, Sowers J., Thaller M.L., 1996, *ApJ*, 469, 884
- Hilditch R.W., Reynolds A.P., Bell S.A., Pollacco D.L., Edwin R.P., 1991, *The Observatory*, 111, 14

- Howarth I.D., Prinja R.K., 1989, *ApJS*, 69, 527  
Lamers H.J.G.L.M., Leitherer C., 1993, *ApJ*, 412, 771  
Leitherer C., 1988, *ApJ*, 326, 356  
Lucy L.B., 1983, *ApJ*, 274, 372  
Lucy L.B., Abbott D.C., 1993, *ApJ*, 405, 738  
Luo D., McCray R., Mac Low M., 1990, *ApJ*, 362, 267  
Miczaika G.R., 1951, *Z. Astrophys.*, 29, 305  
Owocki S.P., 1994, in Balona L.A., Henrichs H.F., Le Contel J.M., eds, *Proc. IAU Symp. 162, Pulsation, Rotation, and Mass Loss in Early-Type Stars*. Kluwer, Dordrecht, p. 475  
Pauldrach A., Puls J., Kudritzki R.P., 1986, *A&A*, 154, 86  
Pearce J.A., 1953, *AJ*, 58, 223  
Pittard J.M., Stevens I.R., 1997, *MNRAS*, 292, 298  
Plaskett J.S., Harper W.E., 1908, *AJ*, 27, 272  
Plaskett J.S., Harper W.E., 1909, *AJ*, 30, 373  
Puls J., 1987, *A&A*, 184, 227  
Puls J., Owocki S.P., Fullerton A.W., 1993, *A&A*, 279, 457  
Raymond J.C., Smith B.W., 1977, *ApJS*, 35, 419  
Savage B.D., Bohlin R.C., Drake J.F., Budich W., 1977, *ApJ*, 216, 291  
Shull J.M., Van Steenberg M.E., 1985, *ApJ*, 194, 599  
Snow T.P., Jr, Cash W., Grady C.A., 1981, *ApJ*, 244, L19  
Sobolev V.V., 1960, *Moving Envelopes of Stars*. Harvard University Press, Cambridge  
Stevens I.R., 1988, *MNRAS*, 235, 523  
Stevens I.R., Pollock A.M.T., 1994, *MNRAS*, 269, 226  
Stevens I.R., Blondin J.M., Pollock A.M.T., 1992, *ApJ*, 386, 265  
Stevens I.R., Corcoran M.F., Willis A.J., Skinner S.L., Pollock A.M.T., Nagase F., and Koyama K., 1996, *MNRAS*, 283, 589  
Stickland D.J., Pike C.D., Lloyd C., Howarth I.D., 1987, *A&A*, 184, 185

This paper has been typeset from a  $\text{T}_E\text{X}/\text{L}^A\text{T}_E\text{X}$  file prepared by the author.